CHEMISTRY OF MATERIALS

ARTICLE

pubs.acs.org/cm

Magnetic Iron Oxide Nanoparticles in 10−40 nm Range: Composition in Terms of Magnetite/Maghemite Ratio and Effect on the Magnetic Properties

Jaime Santoyo Salazar,[†] Lucas Perez,[‡] Oscar de Abril,[§] Lai Truong Phuoc,[†] Dris Ihiawakrim,[†] Manuel Vazquez,[§] Jean-Marc Greneche,[∥] Sylvie Begin-Colin,[†] and Genevieve Pourroy*[,†]

[†]Institut de Physique et Chimie des Matériaux, UMR 7504 CNRS-ECPM-Université de Strasbourg, 23 rue du Loess, BP 43, 67034 Strasbourg Cedex 2, France

[‡]Dept. Fisica de Materiales, Universidad Complutense, 28040 Madrid, Spain

[§]Materials Science Institute of Madrid, CSIC, 28049 Madrid, Spain

[∥]Laboratoire de Physique de l'Etat Condensé UMR CNRS 6087, Université du Maine 72085, Le Mans Cedex 9, France

Supporting Information

ABSTRACT: Magnetic iron oxide nanoparticles in the 10−40 nm size range and with a reduced distribution in size have been synthesized under argon by using ammonium bases R_4NOH (R = CH_3, C_2H_5, C_3H_7) and a hydrothermal treatment. The size is tuned owing to the base to iron ratio and to the length of the alkyl chain R. We precipitate first ferric hydroxides at pH 1.5−2, then ferrous hydroxide at pH 5.5−6. The rapid increase of pH up to basic pH leads to the formation of magnetic iron oxide particles of 12 nm. For [base] to [Fe] ratio above 3.5, a homogeneous growth occurs during further hydrothermal treatment at 250 °C. The higher the quantity of base added and the longer the alkyl chain used, the smaller the particle size produced. For sizes above 20 nm, the Verwey transition at 120 K, characteristic of magnetite, is observed on the field cooling−zero field cooling magnetization curve. The nanoparticles can be described by a core−shell model, that is, a magnetite core surrounded by an oxidized layer close to maghemite. The fractional volume of maghemite increases as the particle size decreases so that below 20 nm, nanoparticles cannot be properly labeled as "magnetite".

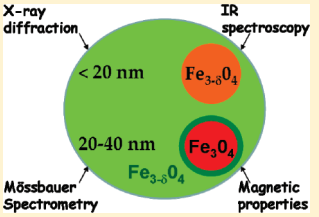

KEYWORDS: magnetite, maghemite, size, core−shell, oxidation, Verwey temperature

1. INTRODUCTION

Magnetic oxides, especially magnetite and maghemite, have been studied for a long time, because of their scientific and technological importance. Nowadays, applications in nanotechnologies are arising, as using the nanoparticles as an elemental block for building electronic devices or as contrast agents for magnetic resonance imaging in medicine.[1−4] Magnetic oxides are also employed as targets for drug delivery and cancer therapy hyperthermia.[3,5,6] The production of monodisperse nanopowders and the control of their composition and size are therefore key points to address for these applications. As an example, hyperthermia applications require particles in the 20−50 nm range, while sizes below 10 nm are appropriate for magnetic resonance imaging (MRI).[7,8] Obtaining narrow particle size distributions in the 10−50 nm range and describing their structure have yet to be achieved. The effects of particle size and surface contribution on the magnetization are not fully understood.[9−11] Furthermore, magnetite (Fe_3O_4) which contains iron in two oxidation states (Fe^{2+} and Fe^{3+}) can be easily oxidized into maghemite (γ-Fe_2O_3), leading to a weaker magnetization. The knowledge of the oxygen content thus appears to be an additional key point.

Two main methods have been developed to obtain magnetite nanoparticles: the decomposition of organometallic precursors such as iron pentacarbonyl,[12] iron(III) cupferronate ($FeCup_3$),[13] or iron(III) acetylacetonate ($Fe(acac)_3$)[14] in the presence of surfactants and the precipitation of Fe^{2+} and Fe^{3+} ions into a basic aqueous media.[15] In the first route, the rate of nucleation and growth and therefore both the size and the size distribution of the particles can be controlled by accurately controlling the reaction temperature and using excess surfactants. Sizes between 2 and 30 nm are currently obtained.[16−18] However, the use of expensive precursors and solvents and the hydrophobic surface generated by the surfactants limit their application particularly in biomedicine; in contrast, the precipitation method allows one to prepare nanoparticles in large quantities, but the size distribution is difficult to control, particularly for sizes higher than 20 nm. Many phases, in particular hydroxides, oxyhydroxides, or oxides, can be stabilized according to the reaction conditions.[19] The elaboration of magnetic fluids by adding ferric and ferrous chlorides to ammonia solution was first reported three decades ago.[20,21] As numerous factors are involved in the precipitation phenomena, great attention has been focused on the under-

Received: May 20, 2010
Revised: January 18, 2011
Published: February 11, 2011

standing of the processes involved and the control of the reaction parameters. It was shown that coprecipitation from a chloride solution heated at 25 °C leads to nanoparticles, the diameter of which decreases from 12 to 4 nm when pH is increased from 8 to 12, while the ionic strength is kept constant.[22,23] The increase of pH and the introduction of ethanol into the reaction leads to a reduction in the particle size. Magnetite nanoparticles of 300 nm in diameter were obtained by adding iron(II) sulfate solution to a base (NaOH) aqueous solution under heating at 90 °C and in the presence of a mild oxidant (KNO_3),[24] or by oxidizing ferrous hydroxide ($Fe(OH)_2$) with a weak oxidant $NaNO_3$ in a N_2-deaerated aqueous NaOH solution (pH = 12−13) at various temperatures below 37 °C.[25] As the synthesis temperature increases from 4 to 37 °C, the magnetic nanoparticles are decreased in size from 102 ± 5.6 to 31.7 ± 4.9 nm and the size distribution increases from 5.5% to 15%.

In the past, the preferred synthesis method involved adding the iron salts to the basic solution, in order to keep the pH constant throughout the reaction. In recent works, the reverse order, that is, the dropwise addition of tetramethyl ammonium hydroxide into the iron (Fe^{2+} and Fe^{3+}) salt solution, causing a rapid increase in pH to a known value, has been used.[26,27] This route produces magnetic nanoparticles of 12 nm in diameter, the composition of which is intermediate between those of maghemite and magnetite. A size increase is observed when subjecting the nanoparticles to a further hydrothermal treatment.[28] Magnetite of 39 ± 5 nm with an overall formula of $Fe_{2.95}O_4$ has been obtained.[29] An accurate characterization of the composition and the structure by using X-ray diffraction, ^{57}Fe Mössbauer spectrometry, and magnetic measurements allows one to conclude that the particles can be ideally described as a magnetite core surrounded by a thin maghemite layer. These nanoparticles can be stabilized in water suspensions when grafted with dendrons and thus are well suited for a further use in biomedical applications.[30]

To increase the range of particle sizes produced, we expanded upon the previous synthesis method by using two other ammonium bases, tetraethyl and tetrapropyl ammonium hydroxide. The increase of the alkyl chain length when compared to tetramethyl ammonium hydroxide in addition to the variation of the quantity of base added permits one to tune the sizes of magnetic iron oxide nanoparticles between 10 and 40 nm. Both the morphology of the resultant nanoparticles and the composition are accurately analyzed by X-ray diffraction, Mössbauer spectrometry, BET, and electron microscopy techniques. One of the most important points deduced from the combination of these techniques and the thermal evolution of the magnetization is that iron oxide nanoparticles with sizes below 20 nm cannot be labeled as "magnetite".

2. EXPERIMENTAL SECTION

2.1. Materials. Iron chloride hexahydrate ($FeCl_3 \cdot 6H_2O$), 99% extra pure, was purchased from Acros Organics, iron chloride tetrahydrate ($FeCl_2 \cdot 4H_2O$) reagent plus 99% from Sigma-Aldrich, hydrochloric acid (HCl) min 37% from Riedel de Häen Sigma Aldrich, and tetramethylammonium hydroxide ($N(CH_3)_4$−OH), 25% w/w, aqua solution from Alfa Aesar; tetraethylammonium hydroxide ($N(C_2H_5)_4$−OH), 20% w/w, aqua solution and tetrapropylammonium hydroxide ($N(C_3H_7)_4$−OH), 20%, w/w, aqua solution were purchased from Fluka.

2.2. Synthesis. All of the solutions were deoxygenated with argon for 30 min. $FeCl_3 \cdot 6H_2O$, 1 M, and $FeCl_2 \cdot 4H_2O$, 2 M, were prepared by dissolving iron salts in HCl, 2 M.[29] A total of 10 mL of the former and 2.5 mL of the latter were mixed and heated up to 70 °C under argon atmosphere, while stirring was maintained. A 1 M solution of base was then injected at 0.7 mL/min, and vigorous stirring was continued for 20 min. The Teflon-lined stainless autoclave was put under an argon atmosphere, and the black suspension was then added under argon. The autoclave was then submitted to a hydrothermal treatment at 250 °C for 24 h and left to cool down to room temperature.

The powders were centrifuged to isolate them from the filtrate. They were washed with distilled water. This procedure was repeated at least four times for each sample until the filtrate had a neutral pH. Finally the powders were lyophilized, stored in an argon atmosphere at 4 °C, and characterized within the following week.

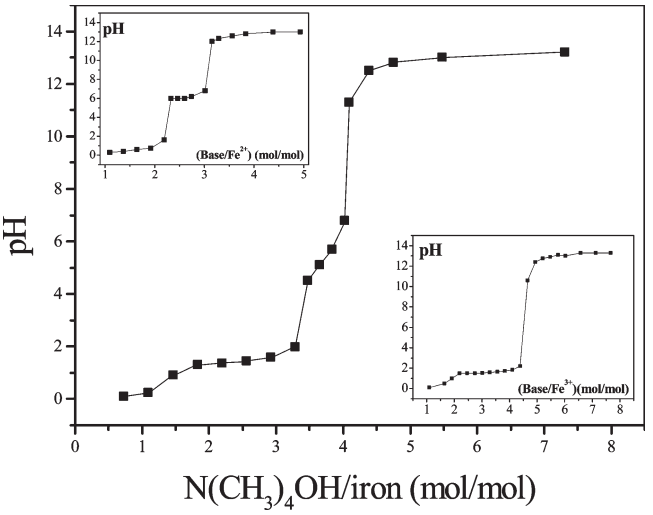

Figure 1. pH versus tetramethyl ammonium to iron ratio (Fe^{3+}: 0.8 M, Fe^{2+}: 0. 4 M, V = 6.25 mL, $N(CH_4)_4OH$: 1 M). The inset exhibits the pH variation during the addition of tetramethyl ammonium into a solution containing Fe^{3+} (bottom right) or Fe^{2+} (top left).

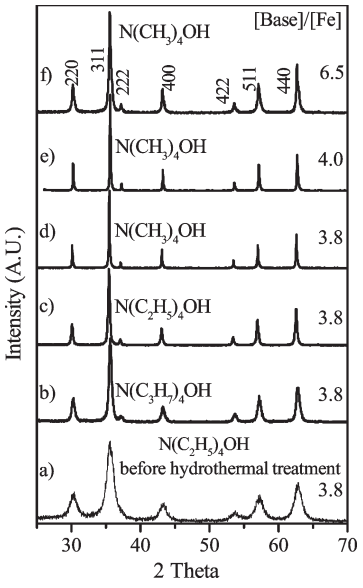

Figure 2. XRD patterns recorded on samples before (a) and after the hydrothermal treatment for the three bases and a base to iron ratio of 3.8 (b−d) and for [$N(CH_3)_4OH$] to Fe molar ratios of 3.8, 4.0, and 6.5 (d−f). The diffraction lines are labeled by *hkl* Miller indices in the spinel structure.

Table 1. Samples Obtained after Hydrothermal Treatment at 250 °C for 24 h with the Three Bases (tetramethyl-, tetraethyl- and tetrapropyl-ammonium)[a]

				X-ray diffraction		specific area		SEM	TEM	M
base	sample	[base]/[Fe]	pH ± 0.5	*a* (nm)	Ø (nm)	(m^2/g)	$Ø_{BET}$ (nm)	Ø (nm)	Ø (nm)	(emu/g)
$(N(CH_3)_4OH)$	S1	3.8	10	0.8395(4)	40(3)	31(1)	38(5)	40(5)	40(5)	84(1)
	S2	4	11	0.8396(1)	35(4)	35(1)	35(5)	35(5)	35(5)	82(1)
	S3	4.8	12	0.8390(7)	22(3)	45(1)	22(5)	23(4)	22(4)	76(1)
	S4	6.5	13	0.8396(3)	23(2)	43(1)	25(5)	23(3)	24(5)	76(1)
$(N(C_2H_5)_4OH)$	S5	3.8	10	0.8392(4)	35(3)	35(1)	35(5)	35(5)	35(5)	82(1)
	S6	4	11	0.8393(3)	25(4)	45(1)	25(1)	25(3)	25(4)	76(1)
	S7	7	13	0.8388(9)	10(4)	10(1)	10(2)	11(4)	10(4)	52(1)
$(N(C_3H_7)_4OH)$	S8	3.8	9.5	0.8389(9)	25(3)	45(1)	25(3)	25(2)	25(5)	76(1)
	S9	4	11	0.8396(6)	20(2)	52(1)	22(3)	20(2)	21(4)	70(1)
	S10	4.3	12	0.8390(7)	15(3)	80(1)	15(1)	15(2)	15(2)	61(1)
	S11	6.5	14	0.8391(6)	12(3)	10(1)	11(2)	12(3)	12(3)	59(1)

[a] Base to iron molar concentration, pH, and particle diameters calculated from X-ray diffraction analysis and specific areas determined by BET method, scanning electron microscopy (SEM), and transmission electron microscopy (TEM). Magnetization (M) measured under 18 kOe at room temperature by using VSM.

Table 2. Effect of Temperature and Duration of the Hydrothermal Treatment on the Particle Size for $(N(CH_3)_4OH)$ and [Base]/[Fe] = 3.8[a]

T (°C)	duration (h)	*a* (nm)	$Ø_{BET}$ (nm)	magnetization (emu/g)
150	24	0.8389(4)	30(5)	77(2)
200	24	0.8392(4)	35(5)	80(2)
250	24	0.8395(4)	40(5)	82(2)
250	6	0.8385(5)	40(5)	82(2)
250	12	0.8390(4)	40(5)	82(2)
250	24	0.8395(4)	40(5)	82(2)

[a] *a* is the lattice parameter and Ø the particle size determined by specific area measurements.

2.3. Characterization. The crystallographic structure of iron oxide nanoparticles was investigated by X-ray diffraction (XRD) using a Bruker D8 Advance diffractometer equipped with a quartz monochromator and Cu Kα radiation (λ = 0.154059 nm). The average diffracting volumes were estimated using the Debye−Scherrer equation, $\Delta(2\theta) = 0.9\lambda/\beta \cos(\theta_0)$ [1] for the (220) and (311) reflections. The lattice parameters a_0 were also calculated from XRD patterns using UFIT[31] and Powder Cell software.[32]

To investigate the morphology, overall views of the powders were recorded by scanning electron microscopy (SEM) using a JEOL electron microscope 6700F coupled with EDX spectroscopy. TEM and HRTEM images were recorded with a TOPCON model 002B transmission electron microscope, operating at 200 kV, with a point to point resolution of 0.18 nm. The size of each particle has been measured on SEM and TEM images by pointing the particle diameter and the distribution of the size has been determined by using ImageJ software. The counting was performed on 150 to 200 particles for each sample.

The specific areas were measured by using the BET method based on the adsorption of a gas monolayer.[33] Assuming a spherical particle shape, the diameter is deduced from the relation $\phi(\text{nm}) = 6000/\mu S$ [2] where ϕ is the particle diameter, μ is the density, and *S* the specific area.

Infrared spectra were recorded from 4000 to 400 cm^{-1} using an IR-spectrometer, DIGILAB FTS 3000 Excalibur series. Samples were gently ground and diluted in nonabsorbent KBr matrixes.

^{57}Fe Mössbauer spectra were performed at 300 K using a conventional constant acceleration transmission spectrometer with a ^{57}Co(Rh) source. The spectra were fitted by means of the MOSFIT program[34] and an α-Fe foil was used as the calibration sample. The values of isomer shift are quoted to that of α-Fe at 300 K.

Hysteresis loops were measured at room temperature using a KLA-Tencor EV7 vibrating sample magnetometer (VSM) under a maximum applied field of 1.8 kOe. The thermal evolution of magnetization was recorded in the temperature range from 5 to 300 K in a Quantum Design superconducting quantum interference device (SQUID) magnetometer under field cooling (FC) and zero-field-cooling (ZFC) conditions. The sample was first cooled from room temperature down to 5 K under an applied field of 8 kOe and then was heated up while magnetization was recorded under a magnetic field of 50 Oe (FC). Subsequently, the sample was demagnetized at room temperature and then cooled down to 5 K under no applied field. Finally, the magnetization was then recorded in a magnetic field of 50 Oe during final heating up (ZFC).

3. RESULTS AND DISCUSSION

3.1. Structure and Morphology. As explained above, the bases are added to the chloride solutions, contrary to the great majority of previously published results on iron oxides synthesized by precipitation, in which the two cations precipitate simultaneously by adding the chlorides to the base, and the pH is basic throughout the reaction. In this study, the powders have been prepared in two steps. Step 1 corresponds to the addition of the ammonium bases to the acidic iron chloride solutions. The pH was measured versus the base to iron ratio ($[N(CH_3)_4OH]/[Fe]$) during the injection of the base (Figure 1). Each point was obtained after a stabilization time of 30 s. For comparison, the insets present the pH variation for solutions containing only Fe^{3+} or Fe^{2+}. After a quasi-linear increase up to pH = 1.5, a plateau occurs corresponding to the precipitation of Fe^{3+} as observed in the bottom right inset. The length of the plateau corresponds to the reaction given by W. Feitknecht et al.,[35] that is, $8Fe[H_2O]_6^{3+} + 22OH^- + 2Cl^- \leftrightarrow [Fe_8O_6(OH)_{10}Cl_2]$. This is followed by dehydration, leading to the precipitation of FeOOH.[36] The rate of pH increase slows down at approximately pH 5−6, corresponding to the Fe^{2+} precipitation. The pH increases again rapidly when the base to iron ratio reaches 3.8 and a black powder precipitates. Each of the three

dx.doi.org/10.1021/cm103188a |*Chem. Mater.* 2011, 23, 1379–1386

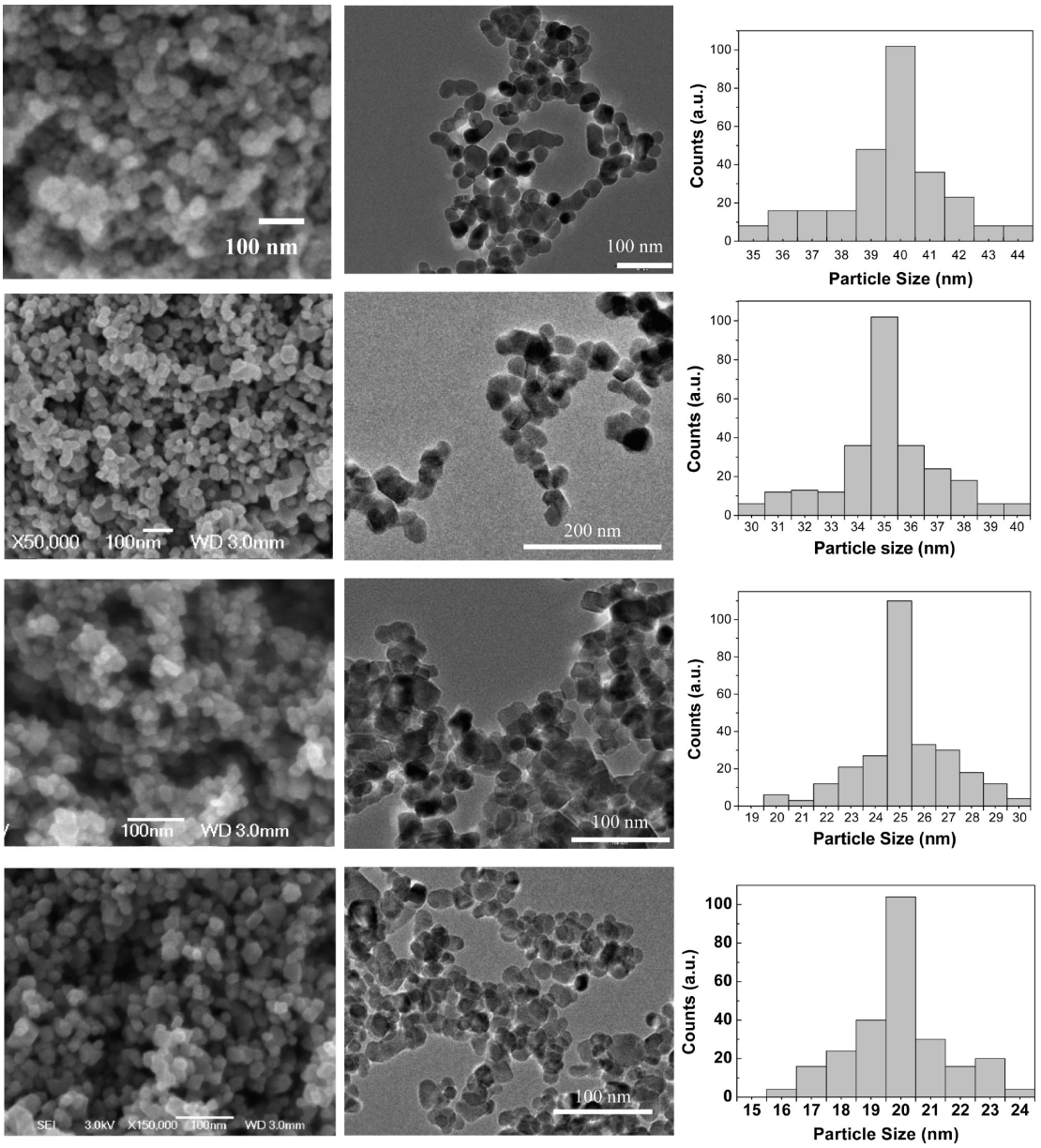

Figure 3. SEM and TEM images of samples S1, S2, S8, and S9 from top to bottom. The size distributions were calculated from TEM image.

ammonium bases used gave the same type of behavior. However, the pH values are slightly higher when tetraethyl- and tetrapropyl-ammonium bases are involved due to the increasing inductive effects of the alkyl chain or when the base solution is more concentrated (Supporting Information S1 and S2). An X-ray diffraction analysis has been carried out on the black powder obtained for base to iron ratios equal or higher than 3.8. All the peaks were indexed in the spinel structure (spatial group $Fd\bar{3}m$ (No. 277), JCPDS No. 19-0629) (Figure 2). Neither hematite nor partially ordered maghemite phases were observed in the pattern. According to previous studies, Fe^{2+} adsorbs at the ferric hydroxide surface. Increasing the pH gives rise to dehydration of hydroxides and leads to the formation of magnetite facilitated by electron hopping between Fe^{2+} and Fe^{3+}.[37−39] The diffraction lines are broad in agreement with previous works.[29] The grain size calculated from the Scherrer formula (relation [1]) is equal to 12(1) nm, and the lattice parameter a = 0.8379 (4) nm is lower than that of microcrystalline magnetite probably due to a slight oxidation when placing it under air.

In a second step, the solutions obtained from base to iron ratios equal to or higher than 3.8 have been submitted to a hydrothermal treatment under argon. After washing and drying, a structural and morphological characterization was undertaken. All the peaks were indexed in the magnetite spinel structure. The lattice parameters are close to the magnetite one (a = 0. 8396 nm) and far from the maghemite one (0.8346 nm, JCPDS file 39-1346) (Table 2). However, the peak width, related to the grain size, varies owing to the nature and the amount of base (Figure 2). It increases when the length of the alkyl chain of the ammonium bases or the base to iron molar ratio increases, suggesting that these parameters have an influence on the grain size.

To investigate the morphology and determine the mean size of the particles, several methods have been used. SEM observations

dx.doi.org/10.1021/cm103188a |*Chem. Mater.* 2011, 23, 1379–1386

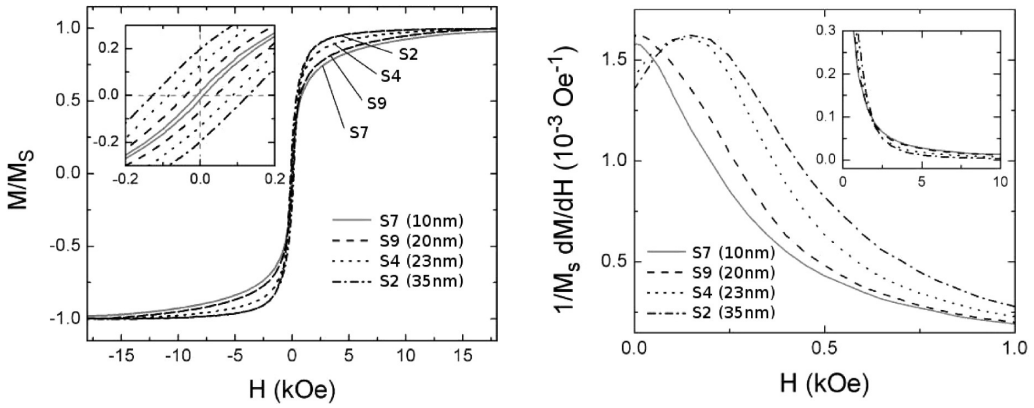

Figure 4. (Left) Hysteresis loops at room temperature for particles with selected size according to the three different regions described in Figure 5. The inset shows the low-field region of the loops. (Right) Differential susceptibility curves are shown corresponding to these loops. Inset shows the curves in the higher field region.

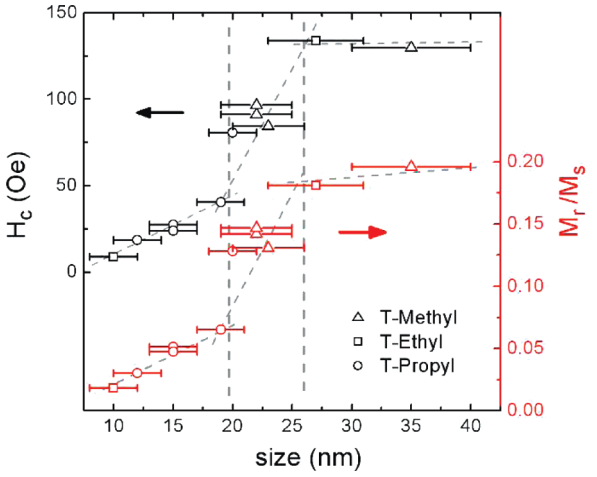

Figure 5. Coercivity and reduced remanence as a function of particle size.

give an overall view on a wide area allowing one to check that no large particles have been produced (Figure 3). TEM observations, the BET method, and X-ray diffraction are three different ways to calculate sizes: the width of diffraction peaks is related to the diffracting volume according to relation [1] and the specific area determined by BET to the size of particles according to relation [2]. The diameters range from 40 and 22 nm for $N(CH_3)_4OH$ and 35 and 10 nm for $N(C_2H_5)_4OH$ to 25 and 12 nm for $N(C_3H_7)_4OH$ (Table 1). The agreement between all techniques shows that the diffracting volume is extended on the whole particle and consequently that the particles are not polycrystalline. Let us note that (1) for identical quantities of base, the particle sizes decrease as the length of the alkyl group of the ammonium base increases; (2) for each base, when the quantity of added base (i.e., pH) increases, the size also decreases. Vayssieres et al. and Horner et al. have also observed a mean size decrease when the pH was increased.[22,28] In addition, we observed an effect of the base addition rate on the final sizes (observed after the hydrothermal treatment). The addition of base was stopped during 30 min at the first plateau (pH = 3) and at pH = 6. No effect was observed in the first case, while broad size dispersions occurred when the addition was stopped for a period at pH = 6. It can be concluded that a rapid pH variation when Fe^{2+} is adsorbed is favorable to the germination step while a slow increase of pH between 6 and 8 favors heterogeneous growths. Otherwise, when pH is kept constant in the 6−8 range, crystallites increase in size. Regarding the hydrothermal treatment and its duration, we observed an increase of the mean size when the temperature increases from 150 °C up to 250 °C for a duration of 24 h (Table 2). The lattice parameter of magnetite is reached after 24 h showing that, for shorter times, the nanoparticles are more oxidized when placing them in air. Probably, a higher temperature of hydrothermal treatment eliminates defaults, hindering the reaction with air at the surface.

3.2. Magnetic Properties. *3.2.1. Magnetization.* To study the magnetic properties of the nanoparticles, samples of the various particles were prepared consisting of a few milligrams of each one in order that all of the samples were equally aggregated. The hysteresis loops of the nanoparticles with different sizes were recorded by VSM at room temperature. The saturation magnetization decreases as the size decreases (Table 1). Normalized hysteresis loops have been drawn for selected particle sizes: S9, S7, S4, and S2 (Figure 4, left). The loops of the smallest particles exhibit very low coercive field and remanence values. This fact indicates that 10 nm diameter particles are very close to behaving as superparamagnets at room temperature, which is consistent with the temperature dependence of its magnetization as will be discussed later.

The evolution of coercivity and remanence is illustrated in Figure 5, where it is observed that both magnitudes exhibit the same increasing trend with the particle size. Their size dependence can be dissected into three regimes: (i) a nearly linear dependence on size for the smaller particles (between 10 and 20 nm), (ii) a steep rise for intermediate sizes (between 20 and 25 nm), and (iii) a much slower variation for particles larger than 25 nm. This difference between the magnetic behavior of small and medium sized particles can also be observed in their hysteresis loops. The approach to magnetic saturation of small particles is much slower (lower susceptibility) and requires much higher applied fields to get them saturated than in the case of larger particles. A change is also observed in the differential magnetic susceptibility (Figure 4, right), whose peaks are shifted toward lower applied fields when the size is reduced. The peak is broader for bigger particles. This change in the size dependence of saturation field and magnetic susceptibility becomes evident

dx.doi.org/10.1021/cm103188a |*Chem. Mater.* 2011, 23, 1379–1386

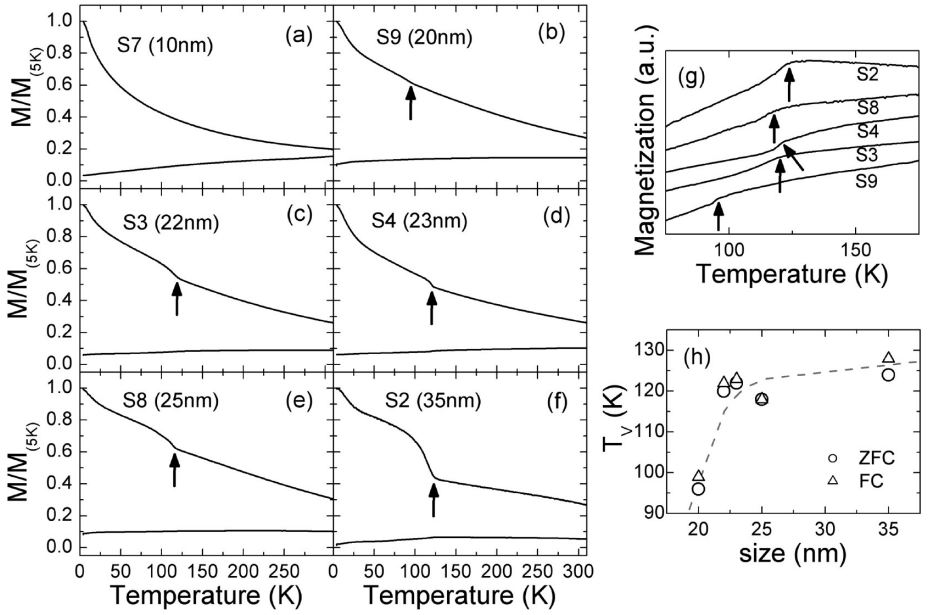

Figure 6. ZFC/FC plots for magnetite nanoparticles of average size (a) 10 nm, (b) 20 nm, (c) 22 nm, (d) 23 nm, (e) 25 nm, and (f) 35 nm. $M_{(5K)}$ corresponds to the magnetization under FC condition at 5 K. (g) Comparison of the ZFC curves around the transition temperature for particles as big as or bigger than 20 nm (magnetization axis scale has been adjusted for every curve for a better comparison). (h) Size dependence of the transition temperature as deduced from both ZFC and FC curves.

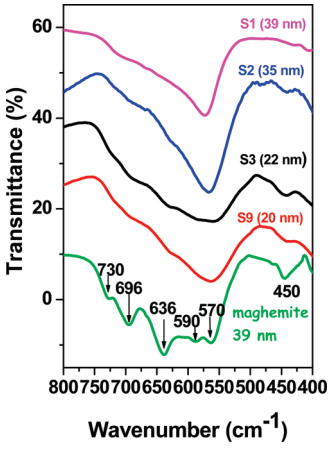

Figure 7. Infrared spectra recorded on samples S1, S2, S3, and S9 and on maghemite obtained by annealing of magnetite under air at 300 °C for 12 h[50].

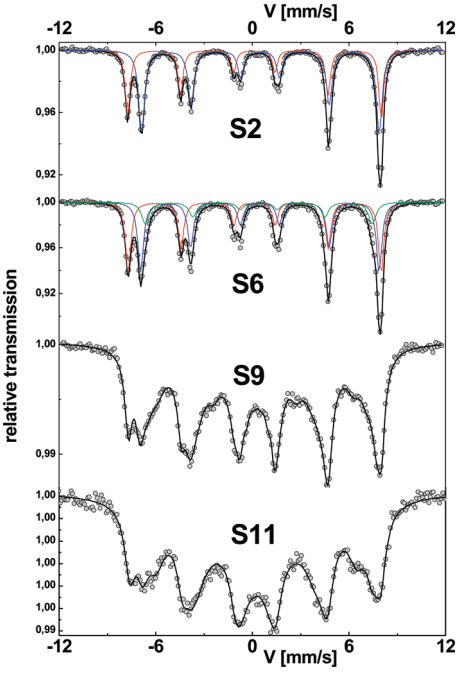

Figure 8. Mössbauer spectra recorded at 300 K on nanoparticle samples.

for values of particle size around 20 nm, in the same way coercivity and remanence do.

3.2.2. Zero Field Cooling/Field Cooling. The ZFC/FC curves are illustrated in Figure 6a−f. They depict the relative magnetization variation $M/M_{(5K)}$ for both FC and ZFC where $M_{(5K)}$ corresponds to the magnetization under FC condition at 5 K. As observed, the ferro- to superparamagnetic transition can be inferred to be above room temperature for all the nanoparticles, and only for nanoparticles of 10 nm in size does such a transition appear to approach room temperature.

A detailed analysis of both FC and ZFC curves gives evidence for a transition, most likely related to the Verwey transition, Tv, which was well established at 120 K for stoichiometric magnetite.[40] The present transition is broad, and the estimation of the temperature remains difficult as indicated by arrows in the FC curves (Figure 6b−f) and in the ZFC curves (Figure 6g). This transition is clearly defined in particles with diameter higher than 20 nm. On the other hand, magnetization in FC curves of particles smaller than 20 nm have a much faster low-temperature decay.

Figure 6h collects the transition temperature values deduced from FC and ZFC curves. A parallel evolution of the transition temperature in FC and ZFC curves is observed, mainly for

dx.doi.org/10.1021/cm103188a |*Chem. Mater.* 2011, 23, 1379–1386

Table 3. Mössbauer Data for Samples with Various Sizes[a]

sample	size (nm)	$\langle B_{hf} \rangle$ $T \pm 0.5$	$\langle IS \rangle$ (mm/s) $\pm$ 0.005	% $Fe_3O_4 \pm 3$	% $Fe_2O_3 \pm 3$	$r_{(Fe_3O_4)}$ nm $\pm$ 0.2	$e_{maghemite}$ nm $\pm$ 0.2
S1	39[29]	47.2	0.507	75	25	17.7	1.8
S2	35	46.8	0.495	77	23	16.0	1.5
S6	25	46.4	0.483	70	30	11.1	1.4
S9	20	35.9	0.424	43	57	7.6	2.4
S10	15	38.0	0.408	34	66	5.2	2.3
S7	10	32.9	0.370	15	85	2.7	2.3

[a] Percentages of magnetite (Fe_3O_4) and maghemite (γ-Fe_2O_3) deduced from the amounts of Fe^{2+} and Fe^{3+}. Corresponding radius of magnetite and thickness of maghemite shell layer assuming a core−shell model.

particles of sizes between 20 and 35 nm. Such a feature can be correlated to the dramatic change of behavior for particles around 20 nm in size as observed by studying the hysteresis loops. That could be related not only to the reduction in size, as other authors have suggested,[41] but also to the composition. Indeed, it has also been reported that small degrees of nonstoichiometry or impurities in magnetite can reduce the Verwey transition temperature dramatically.[42] Another observed effect of the deviation from stoichoimetry is the broadening and reduction of the Verwey transition, observed in FC curves.[43]

3.3. Composition of the Nanoparticles in Terms of the Magnetite/Maghemite Ratio. It is established that fine magnetite particles placed in air at room temperature oxidize to maghemite.[44] Oxidation of Fe^{2+} to Fe^{3+} in magnetite leads to a cation-deficient spinel, and the ferrite ranges from magnetite (x = 0) to maghemite (x = 1/3) according to the formula $[Fe^{3+}]_A[Fe^{2+}_{1-3x}Fe^{3+}_{1+2x}\square_x]_BO_4$ in which $\square$ represents vacancies. The comparison of IR spectra recorded for all of the samples with the spectrum of a partially ordered maghemite confirms the increased oxidation when the size decreases (Figure 7). The spectra exhibit absorption bands around the 570 cm^{-1} characteristic of magnetite. However, the bandwidth increases, and small shoulders in the 600−750 cm^{-1} range as well as a band at 450 cm^{-1} appear when the size decreases. Thus, the appearance of the characteristic maghemite peaks shows that the relative quantity of maghemite increases as the nanoparticles become smaller.

Mössbauer spectrometry is very useful for determining the oxidation state of Fe species. The Mössbauer spectra recorded on larger particles (>20 nm) at 300 K are similar to those usually observed for magnetite (Figure 8). One can unambiguously identify two resolved sextets, one clearly attributed to Fe^{3+} in the A site of spinel magnetite (the outer sextet) while the other one is attributed to Fe ions located in the B site. It is important to emphasize that the values of isomer shift and the respective absorption areas of the two components allow one to establish the mean stoichiometry of the Fe oxide nanoparticle, assuming the isomer shifts of Fe^{3+}_{tetra}, Fe^{3+}_{octa}, and Fe^{2+}_{octa} equal 0.25, 0.40, and 1.00 at 300 K, respectively, and assuming the same recoilless Lamb factor for the different Fe species (Table 3).[45] When the size is lower than 20 nm, the magnetic hyperfine structure is not resolved, consisting of broadened, overlapped, and asymmetrical lines originating from the occurrence of superparamagnetic relaxation phenomena. These were described by means of distribution of a static magnetic hyperfine field slightly correlated to that of isomer shift. The mean stoichiometry can therefore be estimated from the mean isomer shift. Thus, the nanoparticles can be described as magnetite with a slight deviation from stoichiometry. The global formula can be written as $Fe_{3-x}O_4$. The value of the mean isomer shift decreases as the nanoparticle size decreases: such evolution of the electronic density suggests that the amount of Fe^{3+} increases in the oxide. Previous work reported on magnetite nanoparticles of 39 ± 5 nm in size have shown that the nanoparticles consist of a magnetite core surrounded by an oxidized layer close to maghemite.[29] To have a clear image on the oxidation rate of the nanoparticles, we have assumed an ideal case whereby the oxidized layer is maghemite. Taking into account the amount of Fe^{3+}, we have calculated the corresponding thickness of the maghemite shell layer, assuming the presence of spherical particles. They are reported in Table 3: the Fe^{3+} ratio and consequently the quantity of γ-Fe_2O_3 increases when the size decreases. It is greater than 50% when the nanoparticles are below 20 nm and reaches 85% when the diameter is as low as 10 nm. Let us keep in mind that this is an idealized description since the oxidation occurs preferentially at the surface, resulting in a stoichiometry gradient. Accordingly, it can be concluded that the particles studied with diameters below 20 nm are nonstoichiometric magnetite throughout their entire volume.

Therefore, the magnetic properties must be interpreted according to these observations. Magnetite is a ferrimagnetic spinel oxide and, like any magnetic material, can exhibit superparamagnetism, monodomain, or multidomain behaviors depending on the size of the nanoparticles.[46−48] The size limit between superparamagnetism and blocked monodomain behavior depends on the temperature and is about 15−20 nm at room temperature. The monodomain−multidomain transition occurs at about the 40−60 nm diameter range.[49] However, the lack of ideal superparamagnetic behavior observed could be related to dipolar interactions between particles or to the size distribution. It can be concluded that the linear trend of the coercivity and remanence with particle size and the shape of the susceptibility curve itself correspond to the magnetic behavior of nonstoichiometric magnetite particles.

In turn, the steep increase of coercivity and remanence, as well as the change of the susceptibility curve shape, might be related to the stoichiometric/nonstoichiometric magnetite core/shell structure that particles develop above the size of 20 nm. According to this core/shell structure model, the stoichiometric magnetite core of particles of sizes between 20 and 25 nm is very small, which would explain the strong variation of the Verwey transition temperature. However, having a good estimation of the shell thickness for every particle size is very difficult, thus making it impossible to give a realistic quantitative size dependence of the transition temperature.

4. CONCLUSION

Magnetic iron oxide nanoparticles in the 10−40 nm diameter range with a reduced distribution in sizes have been prepared by

using ammonium R_4NOH bases with increasing aliphatic chains length (R = methyl, ethyl, propyl). The size is decreased when the length of the aliphatic chains increases, probably because the adsorption energy on the surface of the nanoparticles is larger for larger molecules. A slow addition of base above pH = 6 strongly affects the final size distribution of the particles. Below 20 nm, these nanoparticles are nonstoichiometric in their whole volume and cannot be labeled "magnetite". The variation of the magnetic properties results from both the size and the composition since the oxidation rate increases as the size decreases. Above 20 nm, the nanoparticles have a core/shell structure, the core being constituted of magnetite, as proved by the observation of the Verwey transition. The shell is an oxidized layer close to maghemite. The magnetic behavior corresponds to that of monodomains of magnetite.

■ ASSOCIATED CONTENT

Supporting Information. The variation of pH versus base to iron molar ratio for the three ammonium bases at a 1 M concentration and versus tetramethyl ammonium to iron ratio for the three concentrations of base are available (PDF). This material is available free of charge via the Internet at http://pubs.acs.org.

■ ACKNOWLEDGMENT

The research leading to these results has received funding from the European Community's Seventh Framework Programme (FP7 2007-2013) under Grant Agreement No. NMP3-SL-2008-214032 and from the Spanish Ministry of Science and Innovation through Project MAT2007-65965-C02-02.

■ REFERENCES

(1) Lin, Y.; Boker, A.; He, J.; Sill, K.; Xiang, H.; Abetz, C.; Li, X.; Wang, J.; Emrick, T.; Long, S.; Wang, Q.; Balazs, A.; Russell, T. P. *Nature* **2005**, *434*, 55.

(2) Laurent, S.; Forge, D.; Port, M.; Roch, A.; Robic, C.; Vander Elst, L.; Muller, R. N. *Chem. Rev.* **2008**, *108*, 2064–2110.

(3) Kim, K.-C.; Kim, E.-K.; Lee, J.-W.; Maeng, S.-L.; Kim, Y.-S. *Curr. App. Phys* **2008**, *8*, 758.

(4) Lima, L., Jr.; Brandl, A. L.; Arelado, A. D.; Goya, G. F. *J. Appl. Phys.* **2006**, *99*, 083908.

(5) Salado, J.; Insausti, M.; Gil del Muro, I.; Lezama, L.; Rojo, T. *J. Non-Cryst. Solids* **2008**, *354*, 5207–5209.

(6) Kikumori, T.; Kobayashi, T.; Sawaki, M.; Imai, T. *Breast Cancer Res. Treat.* **2009**, *113*, 435–441.

(7) Roca, A. G.; Costo, R.; Rebolledo, A. F.; Veintemillas-Verdaguer, S.; Tartaj, P.; Gonzalez-Carreno, T.; Morales, M. P.; Serna, C. J. *J. Phys. D: Appl. Phys.* **2009**, *42*, 224002.

(8) Gazeau, F.; Levy, M.; Wilhelm, C. *Nanomedicine* **2008**, *3* (6), 831–844.

(9) Feng, B.; Hong, R. Y.; Wu, Y. J.; Liu, G. H.; Zhong, L. H.; Zheng, Y.; Ding, J. M.; Wei, D. G. *J. Alloys Compd.* **2009**, *473*, 356–362.

(10) Fortin, J.-P.; Wilhelm, C.; Servais, J.; Menager, C.; Bacri, J.-C.; Gazeau, F. *J. Am. Chem. Soc.* **2007**, *129*, 2628.

(11) Dong-Lin, Z.; Xian-Wei, Z.; Qi-Sheng, X.; Jin-Tian, T. *J. Alloys Compd.* **2009**, *469*, 215.

(12) Hyeon, T.; Lee, S. S.; Park, J.; Chung, Y.; Na, H. B. *J. Am. Chem. Soc.* **2001**, *123*, 12798–12801.

(13) Rockenberger, J.; Scher, E. C.; Alivisatos, A. P. *J. Am. Chem. Soc.* **1999**, *121*, 11595.

(14) Sun, S.; Zeng, H. *J. Am. Chem. Soc.* **2002**, *124*, 8204. Sun, S.; Zeng, H.; Robinson, D. B.; Raoux, S.; Rice, P. M.; Wang, S. X.; Li, G. *J. Am. Chem. Soc.* **2004**, *126*, 273.

(15) Lu, A.-H.; Salabas, E. L.; Schüth, F. *Angew. Chem., Int. Ed.* **2007**, *46*, 1222–1244.

(16) Park, J.; An, K.; Hwang, Y.; Park, J.-G.; Noh, H.-J.; Kim, J.-Y.; Park, J.-H.; Hwang, N.-M.; Hyeon, T. *Nat. Mater.* **2004**, 3.

(17) Guardia, P.; Perez, N.; Labarta, A.; Battle, X. *Langmuir* **2010**, *26*, 5843.

(18) Haitao, Y.; Tomoyuki, O.; Daiji, H.; Migaku, T. *J. Appl. Phys.* **2008**, *103*, 07D526.

(19) Cornell, R. M. Schwertmann, U. *Iron Oxides in the Laboratory*; VCH, Verlagsgesellschaft: Weinheim, 1991.

(20) Khalafalla, S. E.; Reimers, G. W. *IEEE Trans. Magn.* **1980**, *16*, 178.

(21) Massart, R. *IEEE Trans. Magn.* **1981**, *17*, 1247.

(22) Vayssieres, L.; Chaneac, C.; Tronc, E.; Jolivet, J.-P. *J. Colloid Interface Sci.* **1998**, *205*, 205–212.

(23) Jolivet, J.-P.; Froidefond, C.; Pottier, A.; Chaneac, C.; Cassaignon, S.; Tronc, E.; Euzen, P. *J . Mater. Chem.* **2004**, *14*, 3281–3288.

(24) Andres Verges, M.; Costo, R.; Roca, A. G.; Marco, J. F.; Goya, G. F.; Serna, C. J.; Morales, M. P. *J. Phys. D: Appl. Phys.* **2008**, *41*, 134003.

(25) Nishio, K.; Ikeda, M.; Gokon, N.; Tsubouchi, S.; Narimatsu, H.; Mochizuki, Y.; Sakamoto, S.; Sandhu, A.; Abe, M.; Handa, H. *J. Magn. Magn. Mater.* **2007**, *310*, 2408–2410.

(26) Murbe, J.; Rechtenbach, A.; Topfer, J. *Mater. Chem. Phys.* **2008**, *110*, 426–433.

(27) Gnanaprakash, G.; Mahadevan, S.; Jayakumar, T.; Kalyanasundaram, P.; Philip, J.; Raj, B. *Mater. Chem. Phys.* **2007**, *103*, 168–175.

(28) Horner, O.; Neveu, S.; de Montredon, S.; Siaugue, J.-M.; Cabuil, V. *J. Nanopart. Res.* **2009**, *11*, 1247–1250.

(29) Daou, T. J.; Pourroy, G.; Begin-Colin, S.; Greneche, J. M.; Ulhaq-Bouillet, C.; Legare, P.; Bernhardt, P.; Leuvrey, C.; Rogez, G. *Chem. Mater.* **2006**, *18*, 4399–4404.

(30) Daou, T. J.; Pourroy, G.; Greneche, J. M.; Bertin, A.; Felder-Flesch, D.; Begin-Colin, S. *Dalton Trans.* **2009**, *23*, 4442.

(31) Michael E. *Ufit*, Software version 1.3; 1992.

(32) Kraus W.; Nolze G. *Powder Cell Sofware*, version 2.4.

(33) Brunauer, S.; Emmett, P. H.; Teller, E. *J. Am. Chem. Soc.* **1938**, *60*, 309.

(34) Teillet, J.; Varret, F. Unpublished MOSFIT program; Université du Maine; le Mans, France.

(35) Feitknecht, W.; Giovanoli, R.; Michaelis, W.; Muller, M. *Helv. Chim. Acta* **1973**, *56*, 2847.

(36) Schwertmann, U.; Friedl, J.; Stanjek, H. *J. Colloid Interface Sci.* **1999**, *209*, 215.

(37) Lakamp, S; Pourroy, G *Eur. J. Solid State Inorg. Chem.* **1997**, *34*, 295–308.

(38) Tronc, E.; Belleville, P.; Jolivet, J.-P.; Livage, J. *Langmuir* **1992**, *8*, 313–319.

(39) Yutaka, T.; Kazuo, I.; Takashi, K. *J. Chem. Soc., Dalton Trans.* **1983**, 189–194.

(40) Aragon, R.; Shepherd, J. P.; Koenitzer, J. W.; Buttrey, D. J.; Rasmussen, R. J.; Honig, J. M. *J. Appl. Phys.* **1985**, *57*, 3221.

(41) Goya, G. F.; Berquió, T. S.; Fonseca, F. C.; Morales, M. P. *J. Appl. Phys.* **2003**, *94*, 3520.

(42) Aragón, R.; Buttrey, G. J.; Shepherd, J. P. *Phys. Rev. B* **1985**, *31*, 430–436.

(43) Özdemir, O.; Dunlop, D. J. *Geophys. Res. Lett.* **1993**, *20*, 1671–1674.

(44) Topsoe, H.; Dumesic, J. A.; Boudart, M. *J. Phys. (Paris)* **1974**, *35*, C6Mll.

(45) Viart, N.; Pourroy, G.; Greneche, J.-M. *Eur. Phys. J.: Appl. Phys.* **2002**, *18*, 33–40.

(46) Hayashi, K.; Sakamoto, W.; Yogo, T. *J. Magn. Magn. Mater.* **2009**, *321*, 450.

(47) Sun, S.; Zeng, H.; Robinson, D. B.; Raoux, S.; Rice, P. M.; Wang, S. X.; Li, G. *J. Am. Chem. Soc.* **2004**, *126*, 273.

(48) Hong, R. Y.; Li, J. H.; Li, H. Z.; Ding, J.; Zheng, Y.; Wei, D. G. *J. Magn. Magn. Mater.* **2008**, *320*, 1605.

(49) Aharoni, A.; Jakubovocs, J. P. *IEEE Trans. Magn.* **1988**, *24*, 1892–1894.

(50) Daou, T. J.; Greneche, J.-M.; Lee, S.-J.; Lee, S.; Lefevre, C.; Bégin-Colin, S.; Pourroy, G. *J. Phys. Chem. C* **2010**, *114*, 8794–8799.